RSC Advances

PAPER

View Article Online
View Journal | View Issue

Cite this: *RSC Adv.*, 2019, **9**, 34567

A facile and concise route to (hydroxybenzoyl) pyrido[2,3-*d*]pyrimidine heterocycle derivatives: synthesis, and structural, spectral and computational exploration†

Abida Ashraf,[ae] Muhammad Khalid, *[b] Muhammad Nawaz Tahir,[c] Muhammad Yaqub,[a] Muhammad Moazzam Naseer, [d] Ghulam Mustafa Kamal,[b] Bullo Saifullah, [bg] Ataualpa Albert Carmo Braga, [f] Zahid Shafiq*[a] and Waqar Rauf [h]

Received 15th July 2019
Accepted 10th September 2019

DOI: 10.1039/c9ra05415d

rsc.li/rsc-advances

In this work, we report the efficient synthesis of novel (hydroxybenzoyl)pyrido[2,3-*d*]pyrimidine heterocycle derivatives: 6-(2-hydroxy-5-methylbenzoyl)-1-methylpyrido[2,3-*d*]pyrimidine-2,4(1*H*,3*H*)-dione (**6a**), 6-(5-fluoro-2-hydroxybenzoyl)-1-methylpyrido[2,3-*d*]pyrimidine-2,4(1*H*,3*H*)-dione (**6b**), 6-(5-ethyl-2-hydroxybenzoyl)-1-methylpyrido[2,3-*d*]pyrimidine-2,4(1*H*,3*H*)-dione (**6c**) and 6-(2-hydroxy-5-isopropylbenzoyl)-1-methylpyrido[2,3-*d*]pyrimidine-2,4(1*H*,3*H*)-dione (**6d**). The chemical structures of the title compounds were ascertained by spectral techniques including ^{1}H, ^{13}C NMR, UV-visible and FT-IR spectroscopy as well as single-crystal X-ray diffraction analysis. Additionally, density functional theory (DFT) and time-dependent (TD-DFT) computation were adopted to analyze the electronic structures of **6a–d**. Compounds **6a–d** were computed in the ground state for FT-IR spectroscopic and natural bond orbital (NBO) analysis by DFT/B3LYP with the 6-311+G(d,p) basis set. UV-vis spectroscopic and HOMO and LUMO energy values for **6a–d** were determined *via* TD-DFT/B3LYP with the 6-311+G(d,p) basis set. The optimized geometric parameters, UV-vis findings, and vibrational frequencies indicate good consistency with the experimental data. NBO analysis was conducted to explore the interactions and charge transfer among different orbitals in the title compounds. The HOMO and LUMO band gap (ΔE) values for **6a–d** were found to be 3.93, 3.91, 4.10 and 3.91 eV, respectively. Molecular electrostatic potential (MEP) analysis explored the reactivity of the title compounds by predicting their nucleophilic as well as electrophilic sites.

Introduction

Among the synthetic heterocyclic compounds, N-heterocycles have received widespread consideration from researchers in pharmaceutics and drug discovery. Pyridines as common six-membered heterocycles are important building blocks of biologically active and naturally occurring compounds.[1] Pyridopyrimidines represent a wide-ranging class of annulated uracils, which have gained substantial attention over the last few decades owing to the presence of the pyrimidine nucleus, which occurs frequently in nature in nucleic acids, coffee, nucleotides, cocoa, alkaloids from tea and uric acid. Xanthene was the first pyrimidine nucleus-containing compound discovered in bladder stones by Marget in 1817.[2] Owing to the position of the nitrogen atom in the pyridine moiety, there are four possible isomers of pyrido[*d*]pyrimidines.[3] Among these isomers, pyrido[2,3-*d*]pyrimidines are the most abundant as potent inhibitors of adenosine kinase,[4] tyrosine kinase,[5] dihydrofolate reductase **1**,[6] and cyclin-dependent kinase (4) **2**.[7] Moreover, pyrido[2,3-*d*]pyrimidines are molluscicidal, anti-inflammatory

---

[a] *Institute of Chemical Sciences, Bahauddin Zakariya University, Multan 60800, Pakistan. E-mail: zahidshafiq25@hotmail.com*

[b] *Department of Chemistry, Khwaja Fareed University of Engineering & Information Technology, Rahim Yar Khan-64200, Pakistan. E-mail: muhammad.khalid@kfueit.edu.pk; Khalid@iq.usp.br*

[c] *Department of Physics, University of Sargodha, Sargodha, Pakistan*

[d] *Department of Chemistry Quaid-i-Azam University Islamabad, 45320, Pakistan*

[e] *Department of Chemistry, Kutchery Campus, The Women University Multan, Multan 60000, Pakistan*

[f] *Departamento de Química Fundamental, Instituto de Química, Universidade de São Paulo, Avenida Professor Lineu Prestes, 748, São Paulo 05508-000, Brazil*

[g] *Department of Biomedical Engineering, Mehran University of Engineering Technology, Jamshoro, Sindh, 76062, Pakistan*

[h] *National Institute of Biotechnology and Genetic Engineering (NIBGE), P. O. Box 577, Faisalabad, Pakistan*

† Electronic supplementary information (ESI) available. CCDC 1909617–1909620. For ESI and crystallographic data in CIF or other electronic format see DOI: 10.1039/c9ra05415d

and analgesic,[8] anticancer,[9–11] antitumor,[12,13] anti-diarrhea **3**,[14] calcium channel antagonist, and anti-leishmanial agents[15] (Fig. 1).

Owing to their biological prominence, substantial effort has been focused towards synthetic strategies for pharmacologically active pyrido[2,3-*d*] pyrimidines, though there remain many challenges for the synthesis of naturally occurring complex molecules.[2]

In continuation of our research work,[16–20] we have synthesized some bioactive nitrogen- and oxygen-containing (hydroxybenzoyl)pyrido[2,3-*d*]pyrimidine heterocycles. Quantum chemical approaches provided promising insights regarding the chemical and biological systems that often found good agreement with the experimental results. Nowadays, the term "quantum chemical approaches" is used almost synonymously with density functional theory (DFT). DFT calculations provide a reasonable compromise between cost and accuracy. Many scientific publications have revealed that the DFT findings have been in line with experiments.[21] Moreover, DFT-based findings have been recognized as being better than the findings obtained from *ab initio* methods.[22] This might be one of the reasons behind the acceptance of DFT and it is extensively used in different fields of chemistry. Many DFT-based studies have addressed the various structural and mechanistic aspects of chemical systems.[23] In this context, we performed DFT calculations for the molecular geometry to understand the structural parameters, vibrational spectroscopy, NBO analysis for intermolecular interactions and MEP for chemical reactivity surfaces, HOMO–LUMO and nonlinear optics (NLO) analysis for the electronic properties of (hydroxybenzoyl)pyrido[2,3-*d*] pyrimidine heterocycle derivatives.

Experimental

Materials and methods

IR spectra were recorded using a Bruker Alpha FT-IR spectrometer. Melting points were recorded using a Fisher-John melting point apparatus and were uncorrected. UV-visible spectra were recorded using a Shimadzu UV-1800. Proton NMR spectra were recorded using a Bruker (Rheinstetten-Forchheim, Germany) AM 300 MHz spectrometer and ^{13}C NMR spectra were recorded using a Bruker spectrometer at 75 MHz with TMS as the internal standard. Mass spectra were obtained using a Thermo Scientific LTQ-XL system with an electrospray ionization (ESI) source, a JEOL 600 MSRoute, and a JEOL Hx110 mass spectrometer (EI-HR).

General procedure

Synthesis of 6-(2-hydroxybenzoyl)-1-methylpyrido[2,3-*d*] pyrimidine-2,4(1*H*,3*H*)-dione (6a–d). A solution of substituted 3-formylchromone (2 mmol), 6-amino-1-methyluracil (2 mmol) and a catalytic amount of *p*-toluenesulfonic acid in 15 mL of THF was stirred under reflux for an appropriate time at 60 °C. The completion of the reaction was examined by TLC. The yellow solid formed was filtered under hot conditions and washed with hot ethanol to afford the pure product (Scheme 1).

Characterization

6-(2-Hydroxy-5-methylbenzoyl)-1-methylpyrido[2,3-*d*]pyrimidine-2,4(1*H*,3*H*)-dione (6a). Light yellow; yield: 92%; mp: 256–258 °C; ^1H NMR (DMSO-*d6*, 300 MHz): $\delta = 2.52$ (s, 3H, C–CH_3), 3.53 (s, 3H, N–CH_3), 6.90 (d, $J = 8.4$ Hz, 1H, benzyl C_3–H), 7.21 (s, 1H, benzyl C_6–H), 7.29 (dd, $J = 8.4$ Hz, 2.1 Hz, 1H, benzyl C_4–H), 8.42 (d, $J = 1.8$ Hz, 1H, pyridyl C_5–H), 8.97 (d, $J = 1.8$ Hz, 1H, pyridyl C_7–H), 10.13 (s, 1H, OH), 11.93 (s, 1H, NH) ppm; ^{13}C NMR (DMSO-*d6*, 75 MHz) $\delta = 20.3$, 29.1, 111.0, 117.1, 124.6, 128.3, 128.7, 130.7, 134.9, 138.0, 151.0, 154.5, 154.6, 155.0, 161.4, 194.0 ppm; MS: m/z 310.17 $[M - H]^-$; anal. calcd for $C_{16}H_{13}N_3O_4$: C, 61.73; H, 4.21; N, 13.50%; found: C, 61.78; H, 4.24; N, 13.48%.

6-(5-Fluoro-2-hydroxybenzoyl)-1-methylpyrido[2,3-*d*]pyrimidine-2,4(1*H*,3*H*)-dione (6b). Yellow; yield: 77%; mp 214–216 °C; ^1H NMR (DMSO-*d6*, 300 MHz): $\delta = 3.53$ (s, 3H, N–CH_3), 7.00 (dd,

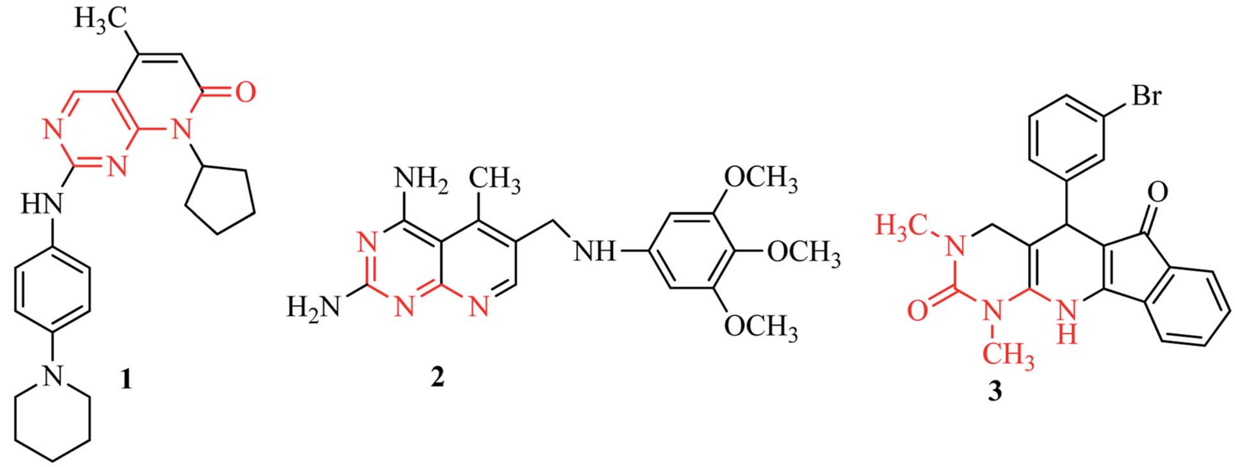

1

2

3

Inhibitor of dihydrofolate reductase

CDK-4 inhibitor

Anti-diarrhea

Fig. 1 Some drugs with a pyridopyrimidine skeleton.

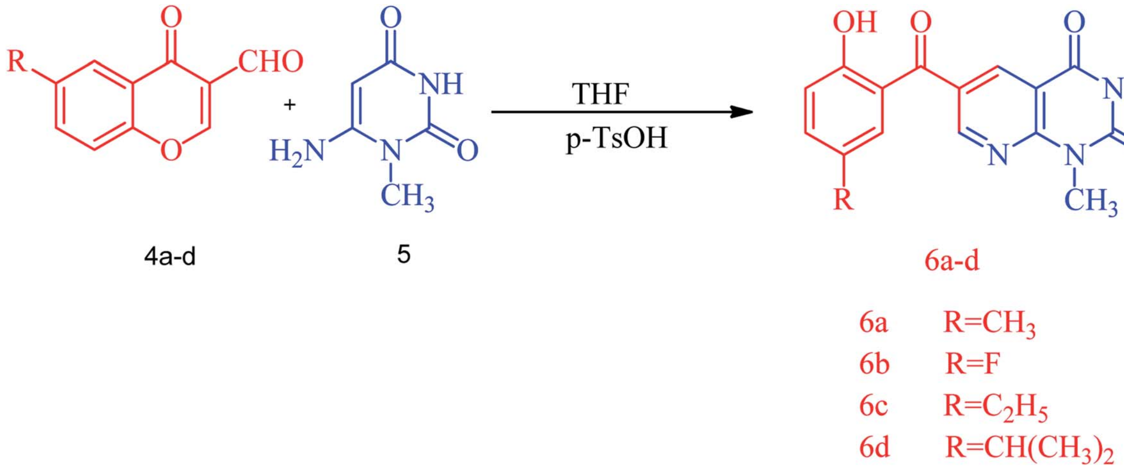

Scheme 1 The synthesis of the pyrido[2,3-*d*]pyrimidine derivatives **6a–d**.

$J = 9.0$ Hz, 4.5 Hz, 1H, benzyl C_3–H), 7.24 (dd, $J = 8.7$ Hz, 3.3 Hz, 1H, benzyl C_6–H), 7.33 (td, $J = 8.7$ Hz, 3.3 Hz, 1H, benzyl C_4–H), 8.43 (d, $J = 2.4$ Hz, 1H, pyridyl C_5–H), 8.99 (d, $J = 2.4$ Hz, 1H, pyridyl C_7–H), 10.26 (s, 1H, OH), 11.95 (s, 1H, NH) ppm; MS: *m*/*z* 314.17 $[M - H]^-$; anal. calcd for $C_{15}H_{10}FN_3O_4$: C, 57.15; H, 3.20; N, 13.33%; found: C, 57.20; H, 3.17; N, 13.29%.

6-(5-Ethyl-2-hydroxybenzoyl)-1-methylpyrido[2,3-*d*]pyrimidine-2,4(1*H*,3*H*)-dione (6c). Yellow; yield: 88%; mp: 270–272 °C; ^{1}H NMR (DMSO-*d6*, 300 MHz): $\delta = 1.16$ (t, $J = 7.8$ Hz, 3H, ethyl CH_3), 2.57 (q, $J = 7.5$ Hz, 2H, benzyl CH_2), 3.53 (s, 3H, N–CH_3), 6.93 (d, $J = 8.4$ Hz, 1H, benzyl C_3–H), 7.24 (d, $J = 2.1$ Hz 1H, benzyl C_6–H), 7.33 (dd, $J = 8.4$ Hz, 2.4 Hz, 1H, benzyl C_4–H), 8.43 (d, $J = 2.4$ Hz, 1H, pyridyl C_5–H), 8.98 (d, $J = 2.1$ Hz, 1H, pyridyl C_7–H), 10.15 (s, 1H, OH), 11.92 (s, 1H, NH); ^{13}C NMR (DMSO-*d6*, 75 MHz) $\delta = 16.1$, 27.5, 29.1, 111.0, 117.2, 124.6, 128.3, 129.6, 133.8, 135.2, 138.0, 151.0, 154.5, 154.8, 155.0, 161.4, 194.0 ppm; MS: *m*/*z* 326.25 $[M + H]^+$; anal. calcd for $C_{17}H_{15}N_3O_4$: C, 62.76; H, 4.65; N, 12.92%; found: C, 62.80; H, 4.63; N, 12.90%.

6-(2-Hydroxy-5-isopropylbenzoyl)-1-methylpyrido[2,3-*d*]pyrimidine-2,4(1*H*,3*H*)-dione (6d). Orange red; yield: 89%; mp 220–222 °C; ^{1}H NMR (DMSO-*d6*, 300 MHz): $\delta = 1.19$ (d, $J = 6.9$ Hz, 6H, isopropyl CH_3), 2.57 (sept, $J = 6.9$ Hz, 1H, benzyl CH), 3.53 (s, 3H, N–CH_3), 6.94 (d, $J = 8.4$ Hz, 1H, benzyl C_3–H), 7.26 (d, $J = 2.1$ Hz 1H, benzyl C_6–H), 7.33 (dd, $J = 8.4$ Hz, 2.4 Hz, 1H, benzyl C_4–H), 8.43 (d, $J = 2.4$ Hz, 1H, pyridyl C_5–H), 8.98 (d, $J = 2.4$ Hz, 1H, pyridyl C_7–H), 10.17 (s, 1H, OH), 11.93 (s, 1H, NH); ^{13}C NMR (DMSO-*d6*, 75 MHz) $\delta =$ 24.4, 29.1, 32.9, 111.0, 117.2, 124.5, 126.0, 128.2, 128.3, 128.5, 132.3, 138.1, 139.8, 151.0, 154.5, 154.9, 155.0, 161.4, 194.0 ppm; MS: *m*/*z* 340.25 $[M + H]^+$; anal. calcd for $C_{18}H_{17}N_3O_4$: C, 63.71; H, 5.05; N, 12.38%; found: C, 63.66; H, 4.98; N, 12.36%.

Computational procedures

The Gaussian 09 program package[24] was used for all the theoretical calculations by employing DFT.[25] The initial geometry was retrieved by using the single-crystal structures of compounds **6a–d**. The geometry of **6a–d** was optimized in the gas phase without following any symmetry restrictions by employing the B3LYP level of theory and the 6-311+G(d,p) basis set. Frequency analysis was used to confirm the ground state structures. No imaginary frequency was there in all cases. Hence, the stability of the optimized structures was ascertained by all the calculated vibrational frequencies. The B3LYP/6-311+G(d,p) level of theory was employed for frontier molecular orbitals (FMOs), NBO, FT-IR and NLO calculations. UV-vis spectra were computed by employing time-dependent density functional theory (TD-DFT) with the B3LYP level and the 6-311+G(d,p) basis set. GaussView 5.0 (ref. 26) was used to organize the input files. The molecular visualization programs Avogadro,[27] Chem Craft[28] and GaussView 5.0 were used to interpret the output file results.

Results and discussion

Chemistry

A series of substituted (2-hydroxybenzoyl)pyridopyrimidines, diverse heterocyclic compounds exhibiting biological importance, have been prepared by reacting substituted 3-formylchromone, 6-amino-1-methyluracil and a catalytic amount of *p*-toluenesulfonic acid in THF under reflux for an appropriate time at 60 °C. The corresponding (2-hydroxybenzoyl)pyrido[2,3-*d*]pyrimidines were obtained as yellow-orange red solids in yields of 77–92%. The reaction was started by the protonation of the formyl group with *p*-toluenesulfonic acid followed by the addition of 6-amino-1-methyluracil to obtain the targeted (2-hydroxybenzoyl)pyridopyrimidine **6a**. The structure of the synthesized compounds was established by spectroscopic data, *i.e.* FT-IR, ^{1}H and ^{13}C NMR. The FT-IR spectra of (2-hydroxybenzoyl)pyridopyrimidines **6a–d** showed characteristic OH and NH stretching frequencies at 3212–3026 cm^{-1} and the C=O stretching was observed in the 1721–1571 cm^{-1} region. The ^{1}H NMR spectra showed two separate singlets at 10.13–10.26 for OH and 11.92–11.95 for NH protons while N–CH_3 protons resonate at 3.52–3.53 ppm. The ^{13}C NMR data for compounds

6a–d also support the IR and ^{1}H NMR data. The plausible mechanism of the reaction is outlined in Scheme S1.†

Crystallographic data collection and structural refinement

Crystals of compounds **6a–d** suitable for X-ray analysis (Table 1) were obtained by slow evaporation of their solutions in THF and MeOH solvent under ambient conditions and were found to have a monoclinic crystal lattice with the $P2_1/n$ space group, a monoclinic crystal lattice with the $P2_1/c$ space group, a triclinic crystal lattice with the $P\bar{1}$ space group and a monoclinic crystal lattice with the $C2/c$ space group, respectively (Table 1).

The information regarding the type of diffractometer, absorption correction and H-atom treatment can be seen in Table S17.† The molecular structures of 6-(2-hydroxybenzoyl)-1-methylpyrido[2,3-*d*]pyrimidine-2,4-diones **6a–d** along with the crystallographic numbering schemes are shown in Fig. 2. As shown in Fig. 2, the benzoyl moiety present at the 6-position of 1-methylpyrido[2,3-*d*]pyrimidine-2,4-dione is tilted from the methylpyrido[2,3-*d*]pyrimidine-2,4-dione plane in **6a–d** with dihedral angles of C(6)–C(8)–C(9)–C(13) = 49.40(2)° in **6a**, C(6)–C(9)–C(10)–C(11) = 30.1(2)° in **6c**, C(1)–C(10)–C(11)–C(15) = −150.19(16)° in **6d** and C(6)–C(7)–C(8)–C(12) = 146.45(14)° in **6b**. In all four compounds, the sigma bond on one side of the central carbonyl that is acting as a bridge between the phenyl and the 1-methylpyrido[2,3-*d*]pyrimidine-2,4-dione rings has frozen rotation owing to the presence of strong intramolecular hydrogen bonds [O(1)–H(1)···O(2), 1.79(3) Å in **6a**; O(1)–H(1)···O(2), 1.89 Å in **6c**; O(1)–H(1)···O(2), 1.89 Å in **6d**; and [O(1)–H(1)···O(2), 1.83 Å in **6b**], whereas the sigma bond on the other side can freely rotate. Owing to this rotation, the substituents present on the hydroxybenzoyl can adopt two arrangements, *i.e. cis* or *trans* to the methyl group present on the pyrido[2,3-*d*]pyrimidine-2,4-dione. In both **6a** and **6c** where the substituents are methyl and ethyl, respectively, on the hydroxybenzoyl moiety, this arrangement is *cis* while it is *trans* in **6d** and **6b** where the substituents are isopropyl and fluorine, respectively, on the hydroxybenzoyl moiety.

An interesting feature of compounds **6a–d** is their molecular packing in the solid state owing to the presence of various hydrogen bond donor and acceptor sites (Fig. 2 and 3). Interestingly, in compound **6a** the amide moiety in pyrido[2,3-*d*]pyrimidinedione interacts with the hydroxybenzyl moiety through hydrogen bonding [N(2)–H(2A)···O(2), 2.00 Å; O(1)–H(1)···O(3), 2.42(2) Å] providing a ten-membered ring rather than forming the centrosymmetric $R_2^{\,2}(8)$ {···H–N–C=O}$_2$ synthon, resulting in 1D zig-zag supramolecular chains. However, this centrosymmetric $R_2^{\,2}(8)$ {···H–N–C=O}$_2$ synthon is observed in both **6c** [N(2)–H(2A)···O(3), 2.02 Å] and **6b** [N(3)–H(3A)···O(4), 1.98 Å]. Interestingly, none of the arrangement observed in **6a**, **6c** and **6b** is present in the solid-state structure of **6d**, most probably owing to the presence of a bulky isopropyl group. The packing of compound **6d** is mainly driven by N–H···O [N(2)–H(2)···O(1), 2.16 Å] and C–H···O [C(6)–H(6)···O(4), 2.496 Å] hydrogen bonds (Fig. 4).

Molecular geometry

The structural parameters of **6a–d** were calculated at the B3LYP level with the 6-311+G(d,p) basis set. The structural parameters resulting from DFT calculations were compared with the

Table 1 X-ray crystallographic data for **6a–d**

Crystal data	**6a**	**6b**	**6c**	**6d**
CCDC	1909617	1909620	1909619	1909618
Chemical formula	$C_{16}H_{13}N_3O_4$	$C_{15}H_{10}FN_3O_4$	$C_{17}H_{15}N_3O_4$	$C_{18}H_{17}N_3O_4$
M_r	311.29	315.26	325.32	339.34
Crystal system, space group	Monoclinic, $P2_1/n$	Monoclinic, $C2/c$	Monoclinic, $P2_1/c$	Triclinic, $P\bar{1}$
Temperature (K)	296	296	296	296
a, b, c (Å)	8.1712 (11), 13.873 (2), 12.3934 (17)	23.336 (3), 6.9240 (6), 17.2853 (18)	11.7250 (5), 13.3565 (6), 10.1992 (4)	8.4030 (4), 9.6898 (4), 10.9110 (7)
α, β, γ (°)	92.098 (6)	108.798 (3)	114.332 (2)	105.870 (2), 98.586 (2), 102.351 (4)
V (Å^3)	1403.9 (3)	2643.9 (5)	1455.37 (11)	814.10 (7)
Z	4	8	4	2
Radiation type	Mo Kα	Mo Kα	Mo Kα	Mo Kα
μ (mm^{-1})	0.11	0.13	0.11	0.10
Crystal size (mm)	0.44 × 0.30 × 0.28	0.44 × 0.38 × 0.30	0.44 × 0.38 × 0.36	0.41 × 0.30 × 0.27
Data collection				
T_{min}, T_{max}	0.940, 0.980	0.930, 0.970	0.930, 0.975	0.940, 0.985
No. of measured, independent and observed [$I > 2\sigma(I)$] reflections	9802, 3315, 2477	8315, 3120, 2521	8838, 3413, 2687	8321, 3154, 2336
R_{int}	0.057	0.031	0.035	0.032
$(\sin\theta/\lambda)_{max}$ (Å^{-1})	0.659	0.658	0.659	0.617
Refinement				
$R[F^2 > 2\sigma(F^2)]$, $wR(F^2)$, S	0.055, 0.172, 1.04	0.043, 0.123, 1.04	0.046, 0.133, 1.05	0.048, 0.156, 1.04
$\Delta\rangle_{max}$, $\Delta\rangle_{min}$ (e Å^{-3})	0.38, −0.28	0.26, −0.19	0.29, −0.20	0.23, −0.23

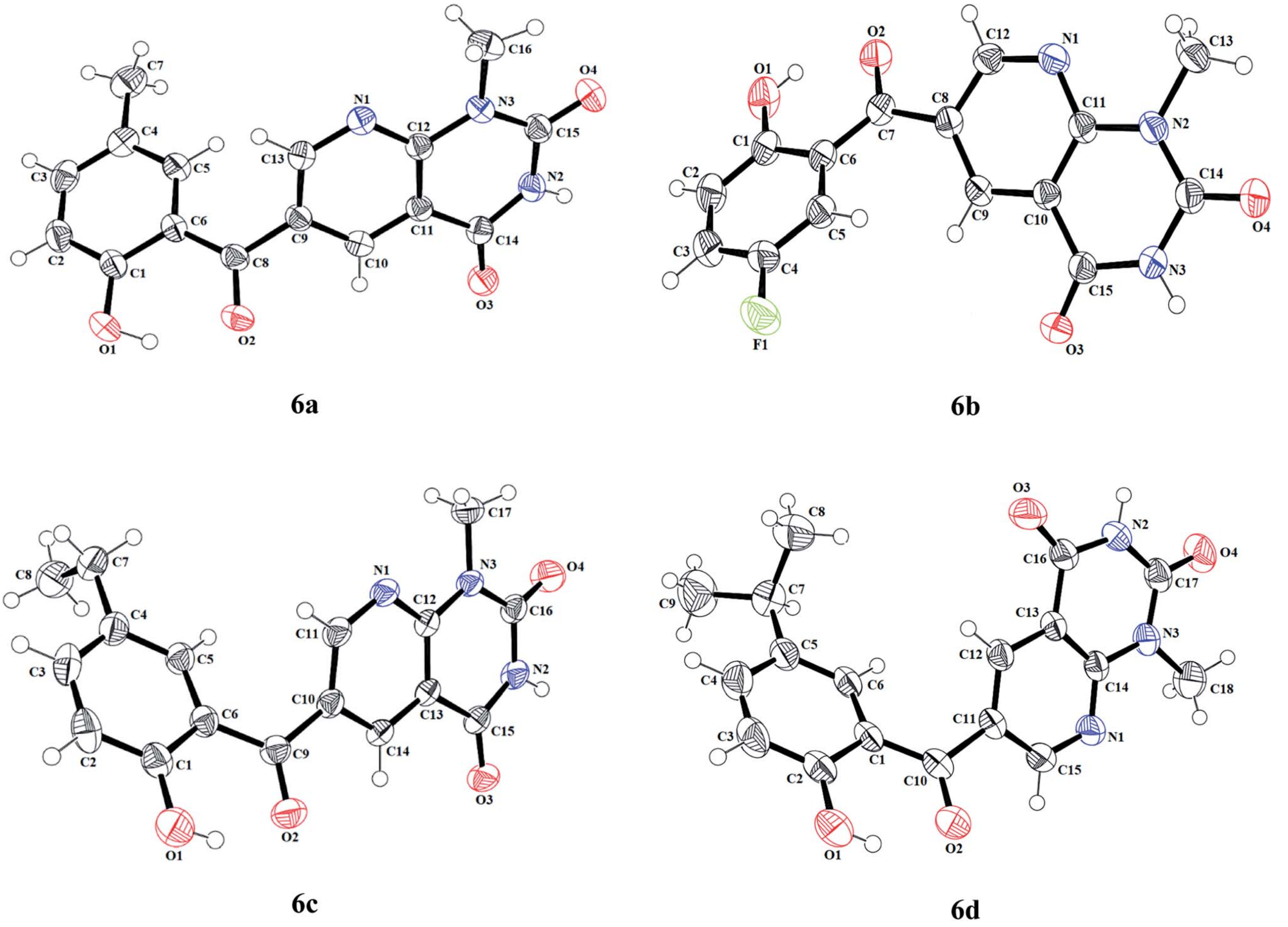

6a

6b

6c

6d

Fig. 2 The molecular structures (ORTEP diagram) of 6-(2-hydroxybenzoyl)-1-methylpyridopyrimidine-2,4-diones **6a–d**. Displacement ellipsoids are drawn at the 50% probability level.

subsequent crystal structural values obtained from XRD analysis. For **6a**, the experimentally determined values for the N1–C13, N2–C14, N2–C15, N3–C12, N3–C15 and N3–C16 bond lengths were 1.334(2), 1.372(2), 1.383(2), 1.385(2), 1.386(2) and 1.464(2) Å, respectively. The DFT values for the aforementioned bond lengths were found to be 1.336, 1.332, 1.391, 1.393, 1.387, 1.395 and 1.470 Å, respectively. The experimentally determined values for the O1–C1, O2–C8, O3–C14 and O4–C15 bond lengths were 1.352(2), 1.235(2), 1.222(2), and 1.209(2) Å, respectively, whereas, the DFT values were calculated to be 1.340, 1.239, 1.214 and 1.213 Å, respectively (Table S1†). The experimentally observed bond angles for O1–C1–C2, O2–C8–C9, O3–C14–N2, C12–N3–C15, O4–C15–N2 and C6–C8–C9 were 117.5(15), 117.2(14), 121.3(15), 122.0(14), 121.3(16) and 121.9(14)°, while the DFT values were found to be 117.8, 122.9, 121.7, 118.0, 121.2 and 121.6°, respectively (Table S1†).

For **6b**, the experimentally determined values of the C–N bond lengths for N1–C11, N1–C12, N2–C11, N2–C14 and N3–C15 were 1.336(18), 1.324(19), 1.384(17), 1.367(19), and 1.378(18) Å, respectively. However, the DFT values of the C–N bond lengths were found to be 1.339, 1.327, 1.386, 1.396 and 1.390 Å, respectively (Table S2†). Further, the experimentally determined values for the O1–C1, O2–C7, O3–C14 and O4–C14 bond lengths were 1.351(18), 1.242(16), 1.212(17) and 1.222(17) Å, respectively, whereas the DFT values of these C–O bond lengths were found to be 1.340, 1.239, 1.215 and 1.212 Å, respectively (Table S2†). The experimentally determined bond angles values for F1–C4–C3, O2–C7–C6, O3–C15–N3, N1–C11–N2, C13–N2–C14 and N3–C15–C10 were 118.2(13), 120.8(12), 121.2(12), 116.7(11), 117.8(12) and 113.9(11)°, while the DFT values for the same angles are 118.8, 120.7, 121.8, 116.8, 118.2 and 113.0°, respectively (Table S2†).

For **6c**, the experimentally determined values for the N1–C11, N1–C12, N2–C15, N2–C16, N3–C12, N3–C16 and N3–C17 bond lengths were 1.332(19), 1.336(17), 1.391(19), 1.393(19), 1.387(18), 1.395(18) and 1.470(18) Å, respectively. The DFT values of the above-mentioned bond lengths were found to be 1.333, 1.337, 1.371, 1.380, 1.383, 1.380 and 1.468 Å, respectively. The experimentally determined values for the O1–C1, O2–C9, O3–C15 and O4–C16 bond lengths were 1.340(2), 1.239(18), 1.214(17) and 1.213(18) Å, respectively. The DFT-based values of the above-mentioned bond lengths (C–O) were 1.349, 1.228, 1.220 and 1.210 Å, respectively (Table S3†). The experimentally determined bond angles observed for O1–C1–C2, O2–C9–C6,

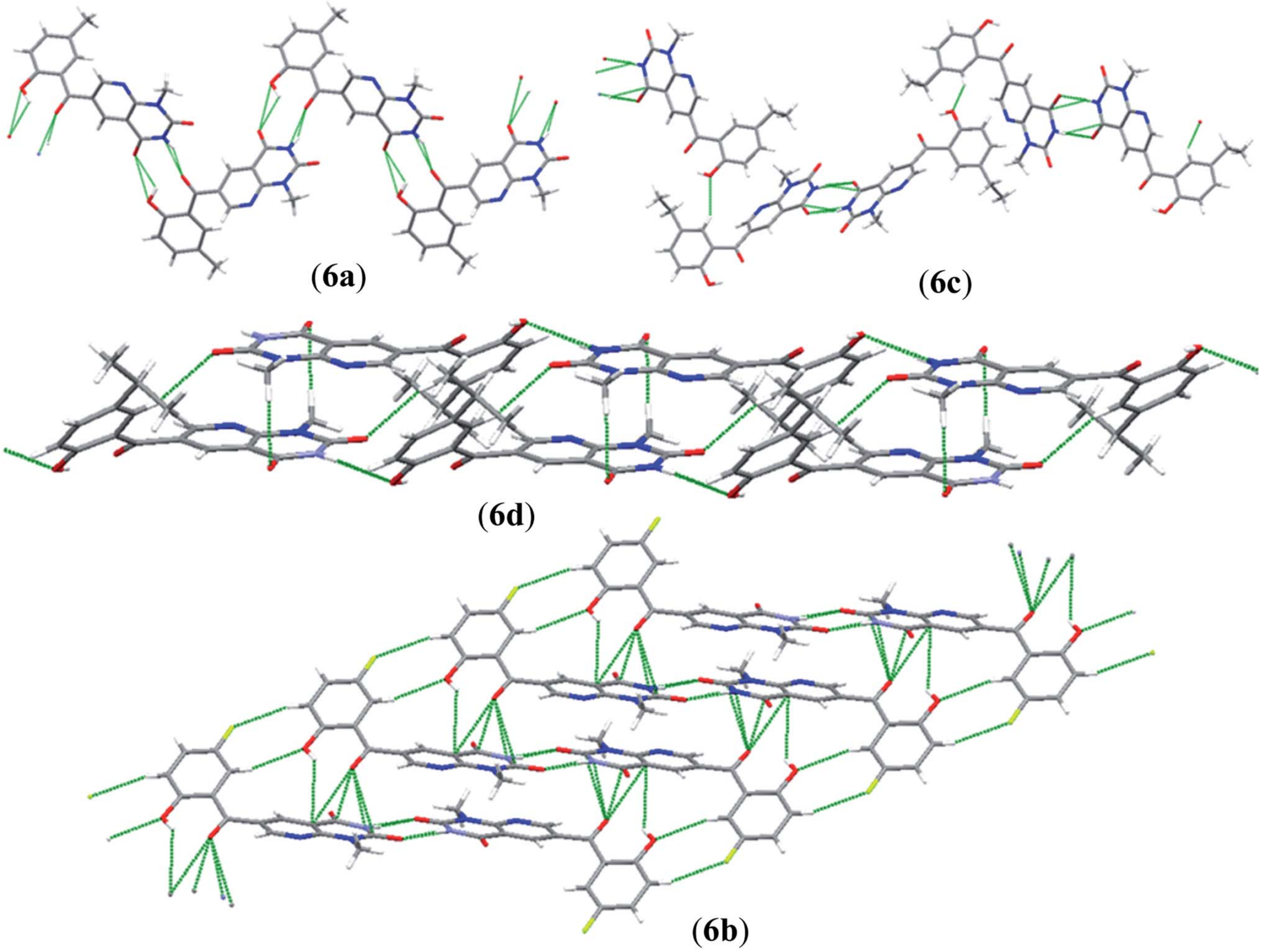

Fig. 3 The hydrogen bond-driven supramolecular chains in **6a–d**.

O3–C15–C13, O4–C16–N3, N1–C11–C10, N2–C16–N3 and C3–C4–C5 were 117.8(14), 121.1(13), 125.4(13), 123.6(14), 124.3(12), 115.2(13) and 117.5(14)° while their DFT values were found to be 117.9, 120.8, 124.1, 122.8, 124.7, 116.2 and 117.1°, respectively (Table S3†).

Furthermore, for **6d**, the experimentally determined values of the N1–C14, N1–C15, N2–C16, N2–C17, N3–C14, N3–C17 and N3–C18 bond lengths were 1.332(2), 1.323(2), 1.368(2), 1.376(2), 1.384 (2), 1.377(2) and 1.462(2) Å, respectively and the DFT values were 1.339, 1.328, 1.390, 1.394, 1.387, 1.395 and 1.471 Å, respectively (Table S4†). The experimentally obtained C–O bond lengths for O1–C2, O2–C10, O3–C16 and O4–C17 were 1.352(2), 1.232(2), 1.210(2) and 1.205(2) Å, respectively, while the DFT values were observed to be 1.341, 1.240, 1.215 and 1.213 Å, respectively (Table S4†). The experimentally determined bond angles for O1–C2–C3, O2–C10–C1, O3–C16–N2, N1–C14–N3, N1–C14–C13 and C2–C3–C4 were 118.3(16), 121.6(16), 121.5(17), 116.7(15), 123.2(16) and 120.7(18)° while the DFT values were 117.8, 121.2, 121.1, 116.8, 122.5 and 120.5°, respectively. The comparative analysis reveals that the experimentally determined bond lengths and bond angles are slightly lower than the calculated parameters, as can be seen in Tables S1–S4.† The observed difference between the DFT and experimental findings might be because of the medium effect. Overall, the obtained structural results for **6a–d** from the DFT and XRD studies show good agreement, as can be seen in Tables S1–S4,† respectively.

FT-IR analysis

The experimental FT-IR absorption spectroscopic studies[29,30] were performed for the vibrational modes of compounds **6a–d**. Further, FT-IR absorption spectroscopic studies based on DFT analysis were also conducted to understand the vibrational modes of compounds **6a–d** using the B3LYP/6-311+G(d,p) level of theory in the gas phase. The vibrational modes were assigned by employing the animation option available in GaussView software. Both the calculated and experimental frequencies are given in Tables S5–S8† for compounds **6a–d**, respectively.

N–H vibrations. The wavenumbers for the nitrogen–hydrogen (N–H) vibrations were located at 3092, 3119–3026, 3131–3045 and 3051 cm^{-1} for **6a–d**, respectively, in

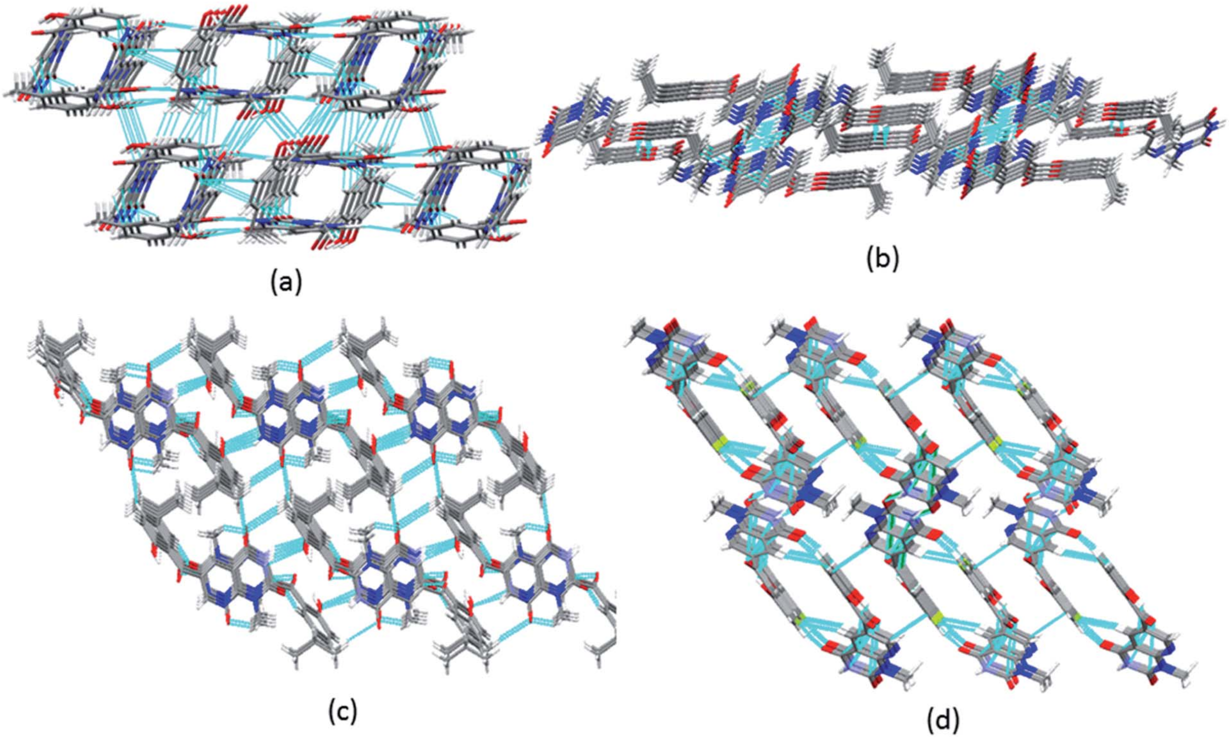

Fig. 4 3D packing of (a) **6a** along the *c*-axis; (b) **6c** along the *b*-axis; (c) **6d** along the *a*-axis; and (d) **6b** along the *b*-axis in the solid state.

experimental FT-IR spectrum which are in agreement with the calculated modes of 3594–3592 cm^{-1} (see Tables S5–S8†).

O–H vibrations. The experimentally determined wavenumbers for the hydroxy (O–H) groups were 3217, 3163, 3168, and 3168 cm^{-1} for **6a–d**, respectively (Fig. S1–S4†); these lower frequencies might be due to intramolecular hydrogen bonding. The simulated bands of the former group were at 3382, 3395, 3385, and 3391 cm^{-1} for **6a–d**, respectively.

C═O vibrations. A strong C═O stretching vibration is found at 1850–1550 cm^{-1}, which is a characteristic carbonyl group peak.[31] The carbonyl (C═O) group bands were located at 1717–1625, 1721–1589, 1685–1628 and 1717–1571 cm^{-1} for **6a–d**, respectively (in the experimental spectra), and 1778–1629, 1780–1768, 1779–1770 and 1778–1632 cm^{-1} for **6a–d**, respectively (in the DFT spectra). Good agreement was observed between the experimental and DFT-based wavenumbers (see Tables S5–S8†).

Natural bond orbital (NBO) analysis

NBO analysis is a significant method for examining intra- and inter-molecular bonding, especially in terms of conjugative and charge transfer interactions between the electron donor and acceptor.[32–39] NBO analysis is helpful in the transmission of electron density from a filled electron orbital to an unoccupied orbital.[40] The stabilization energy can be calculated using eqn (1) with the second-order perturbation approach.

$$E^{(2)} = q_{\mathrm{i}}\frac{(F_{\mathrm{i,j}})^2}{\varepsilon_{\mathrm{j}} - \varepsilon_{\mathrm{i}}} \qquad (1)$$

where $E^{(2)}$ is the stabilization energy, q_{i} is the donor orbital occupancy, $F_{(i,j)}$ is the diagonal and ε_{j} and ε_{i} are the off-diagonal NBO Fock matrix elements.[41]

The value of the perturbation stabilization energy [$E^{(2)}$] depicts the level of conjugation in the whole system. The data for the NBO study regarding molecules **6a–d** was obtained using the B3LYP/6-311+G(d,P) level of theory, as tabulated in Tables S9–S12.† The highest transitions (π → π*) take place as π(N6–C28) → π*(C24–C29) with 43.15 kcal mol^{-1}, π(C11–C19) → π*(C12–C14) with kcal mol^{-1}, π(C6–C30) → π*(C27–C28) with kcal mol^{-1} and π(C10–C11) → π*(C12–C14) with 170.92 kcal mol^{-1} for **6a–d**, respectively. These are the largest values among the stabilization energies given in Tables S9–S12.† The stabilization energy value of **6b** is higher than those for the other compounds **6a**, **6c** and **6d** owing to the stronger intramolecular hyper conjugative interactions, which might be due to the fluoro group. Transitions σ(O1–H2) → σ*(C10–C12), σ(O5–C33) → σ*(C24–C33), σ(C36–H39) → σ*(C36–H39) and σ(C39–H42) → σ*(C39–H42) shown stabilization energy values of 6.07, 65.09, 53.30 and 51.83 kcal mol^{-1} for **6a–d**, respectively. These are the highest σ → σ* stabilization energies in the studied compounds, which result in a strong interaction between the donor (σ) and the acceptor (σ*). In the case of the resonance, the transitions LP(N9) → σ*(O5–C32), LP(N9) → π*(C35–C37), LP(N9) → σ*(C35–C37) and LP(N7) → π*(O4–C37) exhibit stabilization energy values of 70.30, 51.05, 78.19 and 52.43 kcal mol^{-1} for **6a–d**, respectively, as the largest energy values (see Tables S9–S12†). The lowest values of 5.53, 5.88, 5.45 and 7.05 kcal mol^{-1} were exhibited by LP(N6) → σ*(N9–C28), LP(F1) → σ*(C16–C17), LP(N6) → σ*(N9–C30) and LP(N9) →

σ*(C39–C40) in **6a–d**, respectively (see Tables S9–S12†). Subsequently, on the basis of the NBO analysis, it can be concluded that the increased stability in these systems (**6a–d**) is mainly contributed by strong intramolecular hyper conjugative interactions.

Frontier molecular orbital analysis

In order to gain an understanding of the optical properties shown by these compounds, TD-DFT calculations for **6a–d** were carried out at the TD-B3LYP/6-311G+(d,p) level after optimization of their molecular structures for stable spatial conformation. It was realized from SC-XRD findings that the molecular structure of the benzoyl moiety present at position 6 of 1-methylpyridopyrimidine-2,4-dione is tilted from the methylpyridopyrimidine-2,4-dione plane in **6a–d** with the dihedral angles C(6)–C(8)–C(9)–C(13) = 49.40° in **6a**, C(1)–C(10)–C(11)–C(15) = −150.17° in **6b**, C(6)–C(9)–C(10)–C(11) = 30.11° in **6c**, and C(6)–C(7)–C(8)–C(12) = 146.45° in **6d**, which provides some obstruction for the intramolecular charge transfer (ICT) process within **6a–d**. The TD-DFT calculations anticipated that the S0 → S1 transitions are governed through a one-electron transformation from the HOMO to the LUMO. Additionally, according to the TD-B3LYP calculations, the preeminent contributions for the frontier molecular orbitals (FMOs) to the leading transitions in the investigated compounds are shown in Table S13.† The major contribution of the molecular orbitals to the leading transitions is HOMO → LUMO+1 (99%) and HOMO → LUMO (97%) for **6a**. Similarly, the major contribution of the molecular orbitals to the leading transitions is HOMO → LUMO+1 (98%) and HOMO → LUMO (97%) for **6b**. Moreover, the major contribution of the molecular orbitals to the leading transitions is HOMO → LUMO+1 (99%) and HOMO → LUMO (97%) for **6c** and HOMO → LUMO+1 (98%) and HOMO → LUMO (96%) for **6d** (see Table S13†). The FMO diagrams can be seen in Fig. 5–8, which show the electron distribution of the HOMO−2, HOMO−1 and HOMO as well as the LUMO, LUMO+1 and LUMO+2 of molecules **6a–d**. We can see that the electron distribution of the HOMOs of compound **6a** is mainly dispersed over methyl benzoyl moiety, while the LUMO electron distribution is mainly localized over the compound with the exception of the methyl group of the benzoyl moiety and the pyridopyrimidine-2,4-dione moiety (Fig. 5).

For **6b**, the electron distribution of the HOMOs is also mainly dispersed over methyl benzoyl moiety, while the LUMO electron distribution is mainly localized over the whole compound with the exception of the methyl group and the C–N bond of the pyridopyrimidine-2,4-dione moiety as well as only a bit extended on the carbonyl functional group of the pyridopyrimidine-2,4-dione moiety (see Fig. 6).

For **6c**, the electron distribution of the HOMOs is mainly dispersed over the pyridopyrimidine-2,4-dione moiety, while the LUMO electron distribution is are mainly localized on over the pyridopyrimidine-2,4-dione moiety as well as only a bit extended on the carbonyl functional group of the benzoyl moiety (see Fig. 7).

Further, for **6d**, the electron distribution of the HOMOs is mainly dispersed over the methyl benzoyl moiety, while the LUMO electron distribution is mainly localized over the compound with the exception of the methyl group of the benzoyl moiety (see Fig. 8).

Subsequently, this mechanism reveals the existence of ICT character from HOMO to LUMO orbitals.

In addition, the calculated energy values for the HOMO–LUMO and energy gap (E_{gap}) for these compounds are tabulated in Table 2. Subsequently, the energy band gaps (E_{gap}) of the HOMO–LUMO levels for compounds **6a–d** are 3.93 eV, 3.91 eV, 4.1 eV and 3.91 eV, respectively.

The energy gaps of the studied compounds decrease in the following order:

$$\mathbf{6c} > \mathbf{6a} > \mathbf{6b} = \mathbf{6d}$$

The computing calculations show that the electronic properties of the four derivatives might be affected through by the electron donating capability of the substituents, which might

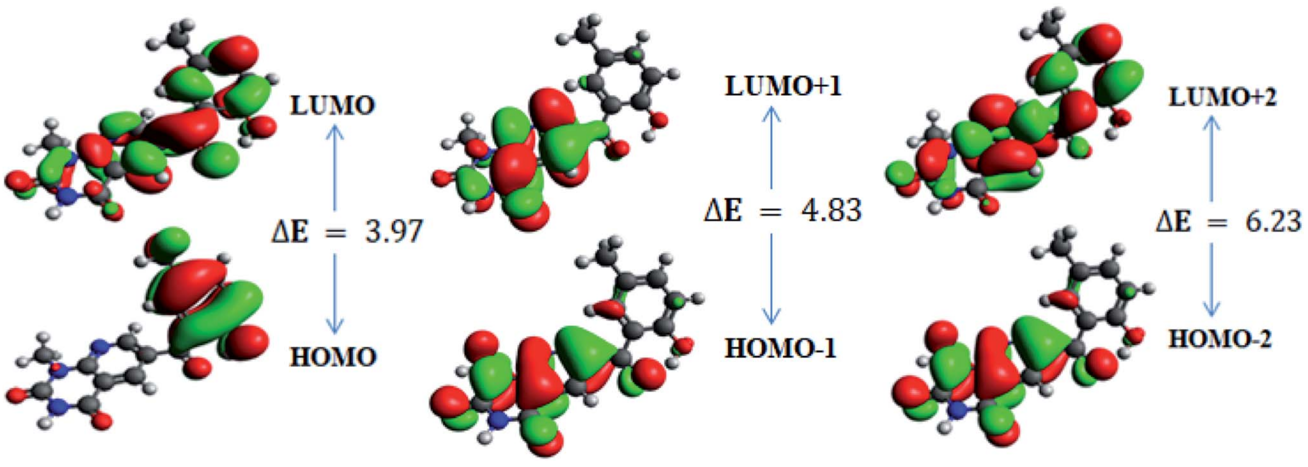

Fig. 5 Frontier molecular orbitals of **6a**.

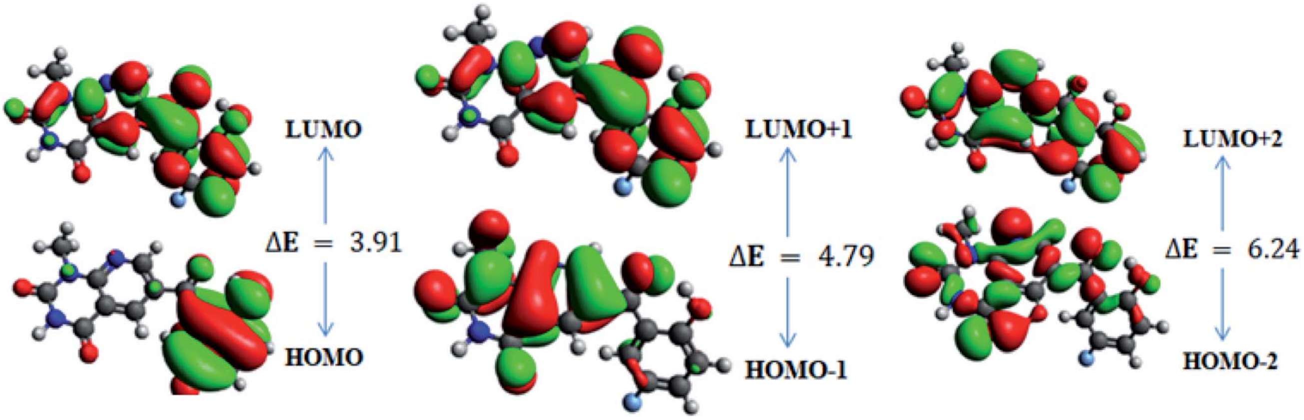

Fig. 6 Frontier molecular orbitals of **6b**.

effectively tune their optical characteristics and the lower E_{gap} explains that the aforesaid derivatives would contain strong electron transfer ability and larger second-order NLO properties.[42,43]

Moreover, the calculated energy values for the FMOs are used for calculating the values of the global reactivity descriptors.[44–47]

The electronic affinity (A) and ionization potential (I) have been calculated in a vertical manner using eqn (2) and (3).

$$I = E_{\text{c}}^{N-1} - E_{\text{o}}^{N} \tag{2}$$

$$A = E_{\text{o}}^{N} - E_{\text{A}}^{N+1} \tag{3}$$

where I = ionization potential; A = electron affinity; E_{c}^{N-1} = cation (energy after losing one electron); E_{o}^{N} = basal state energy (neutral); and E_{A}^{N+1} = anion (energy after gaining one electron).

Hardness and electronegativity values have been calculated using eqn (4) and (5).

$$\eta = \frac{I - A}{2} \tag{4}$$

$$X = \frac{I + A}{2} \tag{5}$$

Electrophilicity calculations were performed to establish the charge transfer process. This describes the relationship between energy variation and the maximum electrons transferred.

$$\omega = \frac{\mu^2}{2\eta} \tag{6}$$

The ability of a chemical species to donate or accept an electron can be explained with the help of two descriptors. eqn (7) and (8) were used to calculate the donating and accepting ability of **6a–d**, respectively.

$$\omega^- = \frac{(3I + A)^2}{16(I - A)} \tag{7}$$

$$\omega^+ = \frac{(I + 3A)^2}{16(I - A)} \tag{8}$$

where, ω^- = electron donating capability; and ω^+ = electron accepting capability.

Eqn (9) was used to calculate the softness value.

$$\sigma = \frac{1}{2\eta} \tag{9}$$

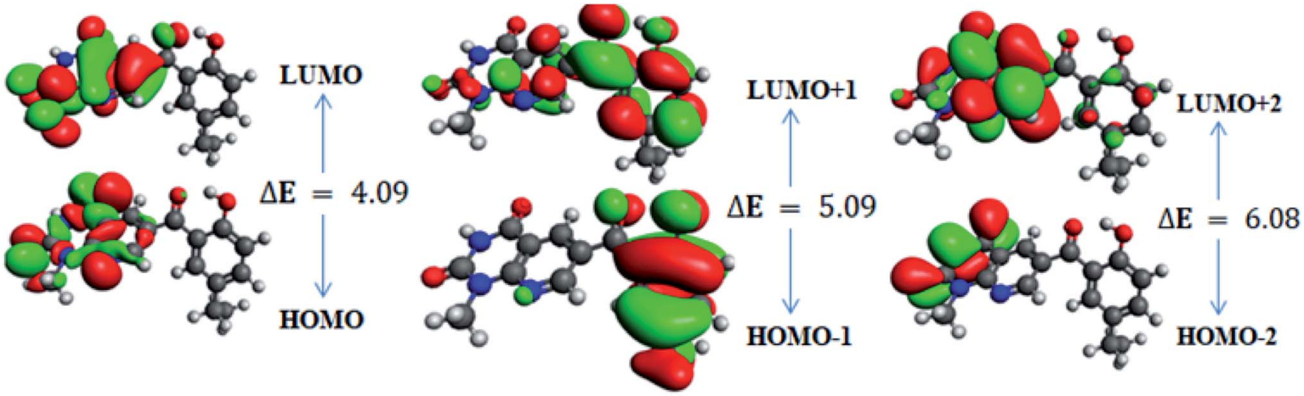

Fig. 7 Frontier molecular orbitals of **6c**.

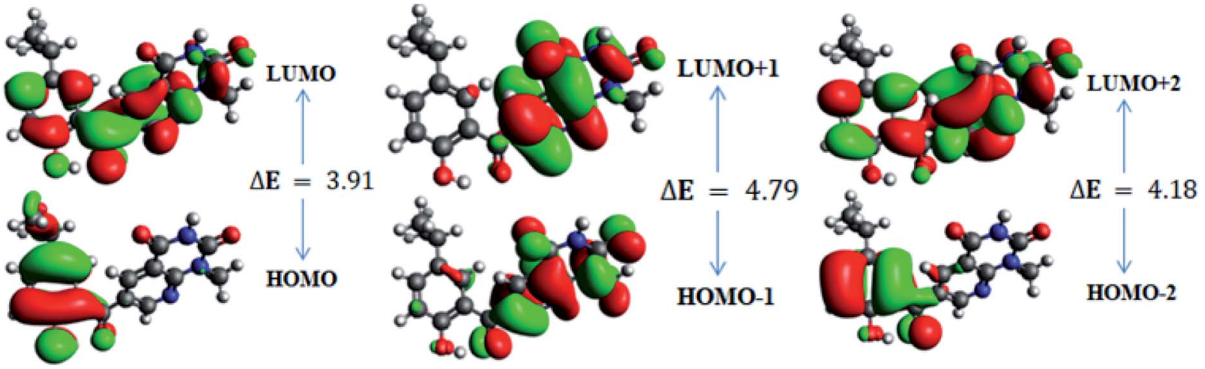

Fig. 8 Frontier molecular orbitals of **6d**.

The results obtained from eqn (2)–(9) are summarized in Table 3.

The highest ionization potential was calculated to be 5.46 eV for **6b**, while the lowest ionization potential was observed for **6a** with a value of 5.19 eV. The ionization potential decreases in the following order: **6b** > **6c** > **6d** > **6a**. The highest electron affinity value was found to be 4.63 eV for **6b**, while the other three derivatives have the same electron affinity of 1.43 eV. The ionization potential and electron affinity can be used to describe the electron releasing and accepting capabilities of the investigated molecules, which are directly related to the energy of the HOMOs and LUMOs. Overall, the ionization potential values are observed to be larger than the electron affinity values, highlighting the better electron donating capability of the investigated molecules (**6a–d**). Usually, a molecule with a high energy gap can be considered as a hard, non-reactive, stable species, and *vice versa*. The global hardness values of our studied systems were found to descend in the following order; **6b** > **6c** > **6d** > **6a** (Table 3). A similar trend is observed for the electronegativity values of the studied compounds (**6a–d**) (Table 3). The chemical potential value of any system can be used to describe its reactivity and stability. Molecules with greater chemical potential values could be considered as less reactive and more stable, and *vice versa*. In decreasing order, the chemical potential values for the studied compounds are: [**6b** ($\mu = -5.04$ eV)] > [**6c** ($\mu = -4.81$ eV)] > [**6d** ($\mu = -4.78$ eV)] > [**6a** ($\mu = -4.62$ eV)].

The global softness values were found to be 2.69, 1.21, 1.30 and 1.41 eV for **6a–d**, respectively. These values have a greater magnitude as compared to their global hardness values. The global electrophilicity (ω) decreases in the following order: **6a** (57.42 eV) > **6d** (32.16 eV) > **6b** (30.79 eV) > **6c** (30.09 eV). In decreasing order, the electron donor capability (ω^-) values are: **6a** (59.75 eV) > **6d** (34.59 eV) > **6b** (33.36 eV) > **6c** (32.55 eV) and the electron acceptor capability (ω^+) values are: **6a** (55.13 eV) > **6d** (29.81 eV) > **6b** (28.32 eV) > **6c** (27.73 eV).

Overall, the electron donating capability (ω^-) values were found to be higher than the electron accepting (ω^+) capability values. The ionization energy and electron affinity values represent the ability of an atom to donate and accept electrons, respectively. In our compounds, the ionization energies were much higher than the electron affinity values, which supports the finding that the electron donating ability (ω^-) of the investigated compounds is higher than their electron accepting ability (ω^+). The aforementioned results show that all investigated molecules have good kinetic stability and electron donating capability.

UV-visible study

The UV-vis absorption spectra of the derivatives (**6a–d**) in acetone, dimethyl sulfoxide (DMSO) and 1, 4-dioxane were recorded at room temperature. DT-DFT UV-vis absorption data were calculated in the gas phase. The UV-visible results for **6a–d** are presented in Table 4.

Table 2 Computed energies (E) for compounds **6a–d**[a]

6a			6b			6c			6d		
MO	Energy	ΔE	MO	Energy	ΔE	MO	Energy	ΔE	MO	Energy	ΔE
HOMO	−6.6	3.93	HOMO	−6.8	3.91	HOMO	−10.6	4.10	HOMO	−6.5	3.91
LUMO	−2.6		LUMO	−2.9		LUMO	−6.5		LUMO	−2.6	
HOMO−1	−7.2	4.8	HOMO−1	−7.3	4.7	HOMO−1	−10.7	5.10	HOMO−1	−7.2	4.78
LUMO+1	−2.4		LUMO+1	−2.5		LUMO+1	−5.6		LUMO+1	−2.4	
HOMO−2	−7.7	6.23	HOMO−2	−7.9	6.24	HOMO−2	−11.2	6.10	HOMO−2	−7.6	6.291
LUMO+2	−1.5		LUMO+2	−1.7		LUMO+2	−5.2		LUMO+2	−1.4	

[a] E = energy; ΔE (eV) = $E_{\mathrm{LUMO}} - E_{\mathrm{HOMO}}$; HOMO, highest occupied molecular orbital; LUMO, lowest unoccupied molecular orbital; MO, molecular orbital.

Table 3 Ionization potential (I), electron affinity (A), electronegativity (X), global hardness (η), chemical potential (μ), global electrophilicity (ω), electron donor capability (ω^-), electron acceptor capability (ω^+) and global softness (σ) values of **6a–d** (units in eV)

Com	I	A	X	η	μ	ω	ω^-	ω^+	σ
6a	4.80	4.43	4.62	0.18	−4.62	57.42	59.75	55.13	2.69
6b	5.46	4.63	5.04	0.41	−5.04	30.79	33.36	28.32	1.21
6c	5.20	4.43	4.81	0.38	−4.81	30.09	32.55	27.73	1.30
6d	5.14	4.43	4.78	0.35	−4.78	32.16	34.59	29.81	1.41

The experimental absorption maxima of **6a** were found to be 332 (acetone), 305 (DMSO) and 300 (1,4-dioxane), while the TD-DFT absorption maxima were found to be 364, 342, 327 and 302 nm in the gas phase with major molecular orbital contributions HOMO → LUMO (97%), HOMO → LUMO+1 (99%), HOMO+4 → LUMO (27%) and HOMO → LUMO+1 (52%), respectively (Table 4). For **6b**, the experimental absorption maxima were found to be 377 (acetone), 300 (DMSO) and 373 nm (1,4-dioxane), while the TD-DFT absorption maxima were found to be 367, 336, 329 and 307 nm in the gas phase with major molecular orbital contributions HOMO → LUMO (97%), HOMO → LUMO+1 (98%), HOMO+4 → LUMO (25%) and HOMO−1 → LUMO (60%), respectively (Table 4). Similarly, for **6c**, the experimental absorption maxima were found to be 332 (acetone), 311 (DMSO) and 305 nm (1,4-dioxane), while the TD-DFT absorption maxima were found to be 367, 343 and 328 nm in the gas phase with major molecular orbital contributions HOMO → LUMO (97%), HOMO → LUMO+1 (98%) and HOMO+4 → LUMO (26%), respectively (Table 4). Further, for **6d**, the experimental absorption maxima were found to be 365 (acetone), 313 (DMSO) and 372 nm (1,4-dioxane), while the TD-DFT absorption maxima were found to be 368, 350 and 327 nm in the gas phase with major molecular orbital contributions HOMO → LUMO (96%), HOMO → LUMO+1 (98%) and HOMO−1 → LUMO (28%), respectively

Table 4 Wavelengths, excitation energies, and oscillator strengths for **6a–d**^{a}

Com	Exp λ (nm)	DFT λ (nm)	E (cm^{-1})	f	MO contributions
6a		364	27 437	0.1408	H → L (97%)
	332^b	342	29 193	0.0017	H → L+1 (99%)
		327	30 522	0.0131	H-4 → L (27%), H-3 → L (29%), H-2 → L (15%), H-1 → L (23%)
	305^c	302	33 156	0.2089	H-1 → L (52%), H-1 → L+1 (27%), H-4 → L (4%), H-3 → L (3%), H-3 → L+1 (3%), H-2 → L (6%)
	300^d	294	34 030	0.0761	H-4 → L+1 (10%), H-3 → L+1 (33%), H-1 → L (13%), H-1 → L+1 (24%), H-3 → LUMO (4%), H-2 → L (9%), H-2 → L+1 (2%)
		292	34 260	0.0399	H-4 → L+1 (10%), H-3 → L+1 (29%), H-1 → L+1 (39%), H-4 → L (4%), H-2 → L (4%), H-1 → L (6%)
6b	377^b	367	27 245	0.1553	H → L (97%)
	373^d	336	29 736	0.002	H → L+1 (98%)
	300^c	330	30 331	0.0282	H-4 → L (25%), H-3 → L (20%), H-2 → L (15%), H-1 → L (33%), H-6 → L (2%)
		307	32 606	0.1772	H-3 → L (14%), H-2 → L (18%), H-1 → L (60%), H-4 → L (5%)
		298	33 599	0.0738	H-1 → L+1 (93%) H-8 → L (2%)
		293	34 114	0.0043	H-2 → L+1 (85%) H-3 → L+1 (3%)
6c	332^b	367	27 347	0.1357	H → L (97%)
	311^c	343	29 155	0.0018	H → L+1 (99%)
	305^d	328	30 511	0.0131	H-4 → L (26%), H-3 → L (33%), H-2 → L (13%), H-1 → L (22%)
6d	372^d	368.198	27 159	0.120	H → L (96%)
	365^b	350.274	28 549	0.002	H → L+1 (98%)
	313^c	327.391	30 544	0.019	H-4 → L (20%), H-3 → L (38%), H-1 → L (28%), H-2 → L (8%)
		298.863	33 460	0.125	H-3 → L (10%), H-1 → L (45%), H-1 → L+1 (35%), H-2 → L (4%)
		298.517	33 499	0.195	H-2 → L (12%), H-1 → L (20%), H-1 → L+1 (55%), H-3 → L (7%)
		292.103	34 234	0.008	H-4 → L+1 (25%), H-3 → L+1 (61%), H-4 → L (3%)

[a] Com = compounds; Exp = experimental; E = Excitation energy; λ = wavelength; f = oscillator strength; MO = molecular orbitals; H = HOMO; L = LUMO; λ (nm). [b] Acetone. [c] DMSO. [d] 1,4-Dioxane.

(Table 4). The maximum absorption bands of the investigated derivatives (**6a–d**) are visibly redshifted, which could be because of the conjugated fused ring system and the influence of the substituents. The bands at the maximum wavelengths might be assigned to the nπ* transitions of the C=C, C=N and C=O bonds of the investigated derivatives (**6a–d**) while the bands at lower wavelengths (~290 nm) might be assigned to the π–π* transitions of the benzene and pyridine rings (Table 4). The UV-visible data reveal good agreement between the experimental and TD-DFT findings.

Nonlinear optical (NLO) properties

Nonlinear optical (NLO) organic molecules have attracted great industrial, current research and academic interest because of their potential applications in the field of optoelectronic technologies.[48] The organic second-order nonlinear optical materials have promising applications in the field of nonlinear optics (NLO) owing to their chemical tunability and choice of synthetic strategies.[49] The sketch of dynamic organic compounds for utilization in NLO response is established on the basis of asymmetric (neocentromeric) polarization. The NLO efficiency could be enhanced by increasing the electron donating and withdrawing groups attached to the π-conjugated system. Therefore, we also studied NLO parameters of the π-conjugated systems at the molecular level (**6a–d**) using the B3LYP level of theory with the 6-311+G(d,p) basis set. In the finite field (FF) method, when a species is placed in a static field (*F*), the resulting energy (*E*) is represented by eqn (10):

$$E = E^0 - \mu_\mathrm{i}F_\mathrm{i} - \frac{1}{2}\alpha_\mathrm{ij}F_\mathrm{i}F_\mathrm{j}F_\mathrm{k} - \frac{1}{24}\gamma_\mathrm{ijkl}F_\mathrm{i}F_\mathrm{j}F_\mathrm{k}F_\mathrm{l} \tag{10}$$

where E_0 stands for the molecular energy in the absence of an electronic field. α represents polarizability, β_tot is the first hyperpolarizability, and γ stands for the second hyperpolarizability, which are calculated by eqn (11)–(13) from the tensors in the *x*, *y* and *z* directions.

$$\alpha = 1/3(\alpha_{xx} + \alpha_{yy} + \alpha_{zz}) \tag{11}$$

$$\beta_\mathrm{tot} = (\beta_x{}^2 + \beta_y{}^2 + \beta_z{}^2)^{1/2} \tag{12}$$

$$\beta_\mathrm{tot} = [(\beta_{xxx} + \beta_{xyy} + \beta_{xzz})^2 + (\beta_{yyy} + \beta_{yzz} + \beta_{yxx})^2 + (\beta_{zzz} + \beta_{zxx} + \beta_{xyz})^2]^{1/2} \tag{13}$$

The first order and the second-order hyperpolarizability for **6a–d**, as well as their component values, are summarized in Tables S15 and S16.†

The first order polarizability along the *x* direction was found to be 346, 331, 355 and 354 a.u. for **6a–d**, respectively. The first order polarizability along the *x* direction is larger than along the *y* and *z* directions (positive directions) for all compounds, which indicates the non-uniform distribution of the charges on the molecules. The total dipole polarizability (α_total) was found to be 238, 223, 251 and 261 a.u. for **6a–d**, respectively (Table S15†). The dipole polarizability magnitudes of **6c** and **6d** are approximately the same but greater than those for **6a** and **6b**. The first order hyperpolarizability was found to be 1144.46, 1468.42, 1103.06 and 1095.34 a.u. for **6a–d**, respectively (Table S16†). The first order hyperpolarizability of **6b** is higher than those for **6a**, **6c** and **6d**, which might be due to the electron withdrawing ability because of the more electronegative fluoro group. Moreover, we compared our obtained parameters for **6a–d** with urea because it is frequently used as a reference molecule for comparative NLO analysis. The first order hyperpolarizability for **6a–d** is remarkably greater than the value for urea ($\beta = 43$ a.u.),[50] which is due to the effect of the extended conjugation in said compounds (Table S16†).

MEP analysis

The reactive sites of molecules **6a–d** have been determined by MEP descriptor. The MEP descriptor is more frequently utilized for the affirmation of the molecular domains that are most suitable susceptible towards nucleophilic and electrophilic attacks.[51] The MEP descriptor is mostly visualized by mapping values on the electron density surface, which is the procedure adopted in our study. MEP surfaces have been displaced in Figure **S5.**† With respect to the displayed MEP surface of molecules **6a–d**, the fluoro, oxygen and nitrogen atoms are considered as sensitive to electrophilic attacks because the MEP surface has the maximal electron density values at these areas. Lower MEP electron density values are situated in the near vicinities of hydrogen atoms and carbon atoms, designating these areas as possibly most sensitive for nucleophilic attacks.

Conclusions

In summary, we synthesized four novel (hydroxybenzoyl)pyrido[2,3-*d*]pyrimidine heterocycle derivatives **6a–d** with the chemical formulas of $C_{16}H_{13}N_3O_4$, $C_{17}H_{15}N_3O_4$, $C_{18}H_{17}N_3O_4$ and $C_{15}H_{10}FN_3O_4$ and good yields of 92%, 77%, 88%, and 89%, respectively. Their chemical structures have been characterized using experimental and sophisticated computational methods. The experimental techniques of ^{1}H NMR, ^{13}C NMR, UV-vis and FT-IR, as well as SC-XRD, were performed to characterize the synthesized derivatives. SC-XRD analysis revealed that **6a–c** crystallized in the monoclinic crystal lattice with the $P2_1/n$, $C2/c$ and $P2_1/c$ space groups, respectively, but **6d** crystallized in a triclinic crystal lattice with the $P\bar{1}$ space group. Spectroscopic findings were found to be quite in line with the SC-XRD data. Further, the quantum chemical-based UV-vis absorption and FT-IR spectra were also found to be quite in line with the SC-XRD and experimental spectroscopic findings. FMO analysis indicated that the studied derivatives are kinetically stable hard compounds with small electron accepting and greater electron donating capabilities. NBO analysis revealed that the increased stability in **6a–d** is mainly contributed to by strong intramolecular hyper-conjugative interactions. Comparative analysis of the NLO properties revealed that **6a–d** have higher NLO values than urea, making them brilliant candidates for hi-tech applications associated with NLO properties. The MEP surfaces of molecules **6a–d** revealed that the fluoro, oxygen and nitrogen atoms are considered sensitive to electrophilic attacks.

Conflicts of interest

The authors declare that they have no conflicts of interest.

Acknowledgements

Ataualpa A. C. Braga (grants # 2011/07895-8, 2015/01491-3 and 2014/25770-6) is thankful to Fundação de Amparo à Pesquisa do Estado de São Paulo for financial support. AACB (grant 309715/2017-2) also thanks the Brazilian National Research Council (CNPq) for financial support and fellowships. This study was financed in part by the Coordenação de Aperfeiçoamento de Pessoal de Nível Superior – Brasil (CAPES) – Finance Code 001.

References

1 M. R. Mohammadizadeh, J. Azizian, F. Teimouri, A. A. Mohammadi, A. R. Karimi and E. Tamari, *Can. J. Chem.*, 2008, **86**, 925–929.

2 M. L. Deb and P. J. Bhuyan, *Beilstein J. Org. Chem.*, 2010, **6**, 11.

3 A. Shamroukh, A. Rashad and F. Abdelmegeid, *J. Chem. Pharm. Res.*, 2016, **8**, 734–772.

4 A. Rajawat, S. Khandelwal and M. Kumar, *Green Chem. Lett. Rev.*, 2014, **7**, 37–45.

5 S. R. Klutchko, H. Zhou, R. T. Winters, T. P. Tran, A. J. Bridges, I. W. Althaus, D. M. Amato, W. L. Elliott, P. A. Ellis and M. A. Meade, *J. Med. Chem.*, 2006, **49**, 1475–1485.

6 J. B. Smaill, B. D. Palmer, G. W. Rewcastle, W. A. Denny, D. J. McNamara, E. M. Dobrusin, A. J. Bridges, H. Zhou, H. H. Showalter and R. T. Winters, *J. Med. Chem.*, 1999, **42**, 1803–1815.

7 M. R. Reddy, B. Akula, S. C. Cosenza, S. Athuluridivakar, M. R. Mallireddigari, V. R. Pallela, V. K. Billa, D. V. Subbaiah, E. V. Bharathi and R. Vasquez-Del Carpio, *J. Med. Chem.*, 2014, **57**, 578–599.

8 N. R. Mohamed, M. M. Abdelhalim, Y. A. Khadrawy, G. A. Elmegeed and O. M. Abdel-Salam, *Steroids*, 2012, **77**, 1469–1476.

9 J. A. Palop, D. Plano, E. Moreno and C. Sanmartín, *ARKIVOC*, 2014, **2**, 187–206.

10 M. M. Gineinah, M. N. Nasr, S. M. Badr and W. M. El-Husseiny, *Med. Chem. Res.*, 2013, **22**, 3943–3952.

11 A. Elgohary and E. E.-A. E. Green, *Sci. J. Chem.*, 2013, **1**, 1–6.

12 S. A. Rostom, G. S. Hassan and H. I. El-Subbagh, *Arch. Pharm.*, 2009, **342**, 584–590.

13 P. Molina, E. Aller, Á. Lorenzo, P. López-Cremades, I. Rioja, A. Ubeda, M. C. Terencio and M. J. Alcaraz, *J. Med. Chem.*, 2001, **44**, 1011–1014.

14 A. Y. Kots, B.-K. Choi, M. E. Estrella-Jimenez, C. A. Warren, S. R. Gilbertson, R. L. Guerrant and F. Murad, *Proc. Natl. Acad. Sci. U. S. A.*, 2008, **105**, 8440–8445.

15 A. Pastor, R. Alajarin, J. J. Vaquero, J. Alvarez-Builla, M. F. de Casa-Juana, C. Sunkel, J. G. Priego, I. Fonseca and J. Sanz-Aparicio, *Tetrahedron*, 1994, **50**, 8085–8098.

16 Q.-u.-N. Tariq, S. Malik, A. Khan, M. M. Naseer, S. U. Khan, A. Ashraf, M. Ashraf, M. Rafiq, K. Mahmood, M. N. Tahir and Z. Shafiq, *Bioorg. Chem.*, 2019, **84**, 372–383.

17 S. Naseem, M. Khalid, M. N. Tahir, M. A. Halim, A. A. C. Braga, M. M. Naseer and Z. Shafiq, *J. Mol. Struct.*, 2017, **1143**, 235–244.

18 M. Yaqub, R. Perveen, Z. Shafiq, H. Pervez and M. N. Tahir, *Synlett*, 2012, **23**, 1755–1758.

19 M. Islam, A. Khan, M. T. Shehzad, A. Hameed, N. Ahmed, S. A. Halim, M. Khiat, M. U. Anwar, J. Hussain, R. Csuk, Z. Shafiq and A. Al-Harrasi, *Bioorg. Chem.*, 2019, **87**, 155–162.

20 M. T. Shehzad, A. Imran, G. S. S. Njateng, A. Hameed, M. Islam, M. al-Rashida, M. Uroos, A. Asari, Z. Shafiq and J. Iqbal, *Bioorg. Chem.*, 2018, **87**, 857–866.

21 E. Taşal, İ. Sıdır, Y. Gülseven, C. Öğretir and T. Önkol, *J. Mol. Struct.*, 2009, **923**, 141–152.

22 A. K. Srivastava, A. K. Pandey, S. K. Gangwar and N. Misra, *J. At. Mol. Sci.*, 2014, **5**, 279–288.

23 F. Neese, *JBIC, J. Biol. Inorg. Chem.*, 2006, **11**, 702–711.

24 M. J. Frisch, G. W. Trucks, H. B. Schlegel, G. E. Scuseria, M. A. Robb, J. R. Cheeseman, G. Scalmani, V. Barone, B. Mennucci, G. A. Petersson, H. Nakatsuji, M. Caricato, X. Li, H. P. Hratchian, A. F. Izmaylov, J. Bloino, G. Zheng, J. L. Sonnenberg, M. Hada, M. Ehara, K. Toyota, R. Fukuda, J. Hasegawa, M. Ishida, T. Nakajima, Y. Honda, O. Kitao, H. Nakai, T. Vreven, J. A. Montgomery Jr, J. E. Peralta, F. Ogliaro, M. Bearpark, J. J. Heyd, E. Brothers, K. N. Kudin, V. N. Staroverov, R. Kobayashi, J. Normand, K. Raghavachari, A. Rendell, J. C. Burant, S. S. Iyengar, J. Tomasi, M. Cossi, N. Rega, J. M. Millam, M. Klene, J. E. Knox, J. B. Cross, V. Bakken, C. Adamo, J. Jaramillo, R. Gomperts, R. E. Stratmann, O. Yazyev, A. J. Austin, R. Cammi, C. Pomelli, J. W. Ochterski, R. L. Martin, K. Morokuma, V. G. Zakrzewski, G. A. Voth, P. Salvador, J. J. Dannenberg, S. Dapprich, A. D. Daniels, Ö. Farkas, J. B. Foresman, J. V. Ortiz, J. Cioslowski and D. J. Fox, *Gaussian 09*, Gaussian, Inc., Wallingford CT, 2009.

25 M. García-Melchor, A. A. Braga, A. Lledos, G. Ujaque and F. Maseras, *Acc. Chem. Res.*, 2013, **46**, 2626–2634.

26 R. Dennington, T. Keith and J. Millam, *Gauss View, Version 5*, Semichem Inc., Shawnee Mission, KS, 2009.

27 Avagadro, http://avogadro.cc/wiki/Main_Page.

28 ChemCraft, http://www.chemcraftprog.com.

29 M. Tammer, *Colloid Polym. Sci.*, 2004, **283**, 235.

30 R. Lu, W. Gan, B.-h. Wu, Z. Zhang, Y. Guo and H.-f. Wang, *J. Phys. Chem. B*, 2005, **109**, 14118–14129.

31 D. N. Sathiyanarayanan, *Vibrational Spectroscopy*, New Age International Publishers, New Delhi, 2004, pp. 424–426.

32 E. D. Glendening, J. Badenhoop and F. Weinhold, *J. Comput. Chem.*, 1998, **19**, 628–646.

33 J. Foster and F. Weinhold, *J. Am. Chem. Soc.*, 1980, **102**, 7211–7218.

34 A. E. Reed and F. Weinhold, *J. Chem. Phys.*, 1983, **78**, 4066–4073.

35 A. E. Reed, R. B. Weinstock and F. Weinhold, *J. Chem. Phys.*, 1985, **83**, 735–746.

36 J. E. Carpenter, *Extension of Lewis structure concepts to open-shell and excited-state molecular species*, University of Wisconsin–Madison, 1987.
37 J. Carpenter and F. Weinhold, *J. Mol. Struct.: THEOCHEM*, 1988, **169**, 41–62.
38 A. E. Reed, L. A. Curtiss and F. Weinhold, *Chem. Rev.*, 1988, **88**, 899–926.
39 F. Weinhold and C. R. Landis, *Chem. Educ. Res. Pract.*, 2001, **2**, 91–104.
40 M. Shahid, M. Salim, M. Khalid, M. N. Tahir, M. U. Khan and A. A. C. Braga, *J. Mol. Struct.*, 2018, **1161**, 66–75.
41 M. Adeel, A. A. Braga, M. N. Tahir, F. Haq, M. Khalid and M. A. Halim, *J. Mol. Struct.*, 2017, **1131**, 136–148.
42 M. Srnec and E. I. Solomon, *J. Am. Chem. Soc.*, 2017, **139**, 2396–2407.
43 F. Kandemirli and S. Sagdinc, *Corros. Sci.*, 2007, **49**, 2118–2130.
44 R. G. Parr, L. v. Szentpály and S. Liu, *J. Am. Chem. Soc.*, 1999, **121**, 1922–1924.
45 R. G. Parr, R. A. Donnelly, M. Levy and W. E. Palke, *J. Chem. Phys.*, 1978, **68**, 3801–3807.
46 P. K. Chattaraj, U. Sarkar and D. R. Roy, *Chem. Rev.*, 2006, **106**, 2065–2091.
47 A. Lesar and I. Milošev, *Chem. Phys. Lett.*, 2009, **483**, 198–203.
48 M. U. Khan, M. Khalid, M. Ibrahim, A. A. C. Braga, M. Safdar, A. A. Al-Saadi and M. R. S. A. Janjua, *J. Phys. Chem. C*, 2018, **122**, 4009–4018.
49 M. U. Khan, M. Ibrahim, M. Khalid, M. S. Qureshi, T. Gulzar, K. M. Zia, A. A. Al-Saadi and M. R. S. A. Janjua, *Chem. Phys. Lett.*, 2019, **715**, 222–230.
50 C. Qin and A. E. Clark, *Chem. Phys. Lett.*, 2007, **438**, 26–30.
51 I. Javed, A. Khurshid, M. N. Arshad and Y. Wang, *New J. Chem.*, 2014, **38**, 752–761.